Applied Catalysis B: Environmental 148–149 (2014) 394–405

Contents lists available at ScienceDirect

Applied Catalysis B: Environmental

journal homepage: www.elsevier.com/locate/apcatb

Competitive role of structural properties of titania–silica mixed oxides and a mechanistic study of the photocatalytic degradation of phenol

Shivatharsiny Rasalingam[a], Harrison S. Kibombo[a], Chia-Ming Wu[a], Rui Peng[a], Jonas Baltrusaitis[b], Ranjit T. Koodali[a,*]

[a] Department of Chemistry, University of South Dakota, 414 E, Clark Street, Vermillion, SD 57069, USA
[b] PhotoCatalytic Synthesis Group, University of Twente, Enschede, The Netherlands

ARTICLE INFO

Article history:
Received 8 August 2013
Received in revised form 8 November 2013
Accepted 14 November 2013
Available online 22 November 2013

Keywords:
Photocatalysts
Titania–silica
Phenol
Heterolinkages
Crystallinity

ABSTRACT

TiO_2–SiO_2 mixed oxide materials were hydrothermally synthesized and the photocatalytic degradation of phenol under UV-irradiation was evaluated. We also demonstrated that varying the co-solvent, modulates the structural properties of the materials. In particular, the use of non-polar co-solvents such as toluene seemed to increase the crystallinity, surface area, and pore diameter while the crystallite size of titania seemed to change little. A comprehensive characterization using surface and bulk techniques evidenced the role of porosities, crystallinity, and Ti–O–Si linkages of the mixed oxides as significant factors that contribute to the degradation of phenol. The TiO_2–SiO_2 mixed oxide material prepared using only ethanol as the solvent showed 24% degradation of phenol after 120 min of irradiation whereas other mixed oxide materials degraded phenol more efficiently (57% to 100%) in the same duration of time. The higher photocatalytic activities of the mixed oxide materials prepared using non-polar solvents is attributed to a combination of factors that include higher Apparent Surface Coverages of Ti–O–Si heterolinkages, larger pore sizes, and most importantly higher crystallinities of the titania phase. Larger pore sizes enabled better transport of reactant molecules and products to and from the active sites (Ti–O–Si heterolinkages) and the higher crystallinities of the titania phase helped in minimizing the electron–hole recombination in these photocatalysts, and thus resulted in high degradation efficiencies.

1. Introduction

Persistent pollution of our hydrosphere is one of the major socio-economic challenges in the world today. The existing techniques employed to curb pollution are energy inefficient and are still prone to the formation of secondary toxic intermediates and by-products that may require intricate procedures for remediation. Organics such as phenol and phenolic compounds are major components of a myriad of industrial chemicals and as such have a prevalence in waste water [1]. Ingestion of excess amounts of phenol poses a threat to organ and tissue functions and thus there is an impetus for their complete removal from water sources for human consumption [2–4].

The advanced oxidation process (AOP), however, has emerged as an attractive technology that promises a renewable and energetically sustainable approach through which the complete mineralization of highly toxic organic compounds such as aromatics, pesticides, petroleum constituents, and volatile organic compounds in water can be achieved [5–7]. AOP techniques for water purification are mainly based on the hydroxyl radical (·OH) formation and their eventual reactivity with the organic molecules. Jaeger and Bard [8] evidenced the presence of ·OH radicals in irradiated aqueous suspensions of titanium dioxide (TiO_2) based composites using spin trapping agents *via* electron spin resonance spectroscopy, and several investigators later credit these highly reactive species as responsible for the degradation of organic molecules [2,7,9]

TiO_2 has been widely used as a photocatalyst for pollutant degradation due to its photochemical stability, low toxicity, and relative affordability [10]. However, because of the notion that limited efficacy of the semiconductor may be related to its low surface area and hydrophobicity, several investigators have opted to incorporate TiO_2 in supports such as silica [11–14], alumina [12], zeolite [15–17], and activated carbon [15,18] etc. to enhance the efficiency, mechanical, and thermal stability. Even though most of the mixed materials show good efficiency, silica is a popular support of choice because it is inert, transparent to UV light, porous, and can facilitate the dispersion of photocatalysts. In numerous literature studies, improved dye adsorption has been attributed to increased hydrophobicity due to the presence of a silica supporting phase. This has prompted the premise that the hydrophobic phase improves adsorption capacities and consequently enhances

* Corresponding author. Tel.: +605 677 6189; fax: +605 677 6397.
E-mail address: Ranjit.Koodali@usd.edu (R.T. Koodali).

0926-3373/$ – see front matter © 2013 Elsevier B.V. All rights reserved.
http://dx.doi.org/10.1016/j.apcatb.2013.11.025

the catalytic activity of TiO_2 based mixed oxides for all organic substrates [11,12]. This may not universally hold truth as demonstrated in this study. Elsewhere, the addition of SiO_2 phase to TiO_2 does not only prevent the phase transformation from anatase to potentially inactive rutile, but it also facilitates in the effective dispersion of the anatase crystallites [19,20] that serve as photoactive centers essential for the cleavage of organic pollutants and their degradation to innocuous intermediates and by-products [21].

Several elaborate methods have been implemented for the preparation of TiO_2–SiO_2 mixed oxides such as flame hydrolysis, and chemical vapor deposition (CVD); however, the sol–gel process provides an avenue through which structural features can be tuned by simply optimizing the synthesis recipe to achieve materials of enhanced properties [11,22–24]. In a recent publication, we successfully explored the effect of various co-solvents on the physicochemical properties of hydrothermally synthesized TiO_2–SiO_2 mixed oxide materials, and revealed that introduction of aromatic co-solvents such as benzene, toluene, and *p*-xylene induces the gelation rate, expands the pore cavities, and results in materials of high surface area due to minimized surface tension of the pore walls [25]. The type of co-solvent used in the synthesis of the material modulates the porosities resulting in varied diffusion properties of reactant and product molecules accessing and leaving the pores, respectively, hence resulting in varying activities at the initial stages of the reaction. This new work extends and conceptualizes the role of textural properties in providing a detailed mechanistic study for the identification of degradation products formed during the photocatalytic degradation of phenol. UV illumination of the semiconductor photocatalyst results in the formation of charge carriers (electrons and holes) that eventually form highly reactive oxidation species (ROS) [26–28] such as ·OH, O_2^{-}·, ·OOH, HOOH, or OH^- [29–31]. At a constant light intensity, catalyst amount, temperature, and solution pH, the concentration of all intermediates formed during the degradation process were quantified by using high performance liquid chromatography (HPLC) in this study.

Titania-silica materials have been widely studied for a variety of catalytic reactions involving selective oxidation, cumene dealkylation, 2-propanol dehydration, 1,2-dichloroethane decomposition, phenol amination etc. [32]. Thus, the unique chemical and physical properties exhibited by titania–silica provide a basis for the fundamental understanding of structure–activity relationship in mixed oxide systems. TiO_2 supported on silica has been extensively investigated for the degradation of a variety of dyes [11,12,33–35], non-aromatics [36–38], pesticides [39,40], and benzyl compounds [14,41,42] in aqueous phase reactions. Although TiO_2–SiO_2 photocatalysts have been also employed for photocatalytic degradation of phenol [13,14,30,31,43–46], existing literature have only examined the effects of the particle size of titania and its loading, and lack several key factors that includes: (i) a systematic and thorough characterization of the surface properties of the TiO_2–SiO_2 materials, (ii) comprehensive and detailed investigation of textural properties of the TiO_2–SiO_2 materials to understand the role of porosities, (iii) effect of Ti–O–Si heterolinkages towards the degradation of phenol, (iv) detailed identification and quantitative analysis of the reaction intermediates and photodegradation products, and (v) elucidation of the reactive oxidative species that are responsible for the degradation process.

In addition, some earlier reports reported kinetics and product identification of phenol degradation by TiO_2 and metal doped TiO_2 [47–49], but such studies pertaining to the mechanistic pathways using titania–silica photocatalysts are still missing in the literature, and is the motivation for this work. We thus provide new knowledge implicating Ti–O–Si hetero linkages, pore sizes of the materials, and crystallinity as factors that optimally contribute to the overall photocatalytic efficiencies in TiO_2–SiO_2 mixed oxide materials.

2 Experimental

2.1 Materials and preparation

Commercially available tetraethylorthosilicate (TEOS, Acros 98%), titanium isopropoxide (Ti(^{i}OPr)$_4$, Acros 98 + %), anhydrous ethanol (EtOH, Pharmco-AAPER, ACS/USP grade, 200 proof), conc. nitric acid (HNO_3), pentane, hexane, nonane, benzene, toluene, *p*-xylene (all ACS grade) were used as received to prepare the TiO_2–SiO_2 mixed oxides. Phenol (Acros, 99 + % ACS grade), hydroquinone (Sigma, >99%), maleic acid (Alfa Aesar), acetic acid (Fisher), fumaric acid (Acros), pyrogallol (Alfa Aesar, 99% ACS Grade), catechol, and methanol (Acros, 99.9% HPLC grade) were purchased and used for the HPLC studies without further purification. triethanolamine (TEA, Acros, ACS grade), sodium hydroxide (Acros), terephthalic acid (TPA, Acros, 98%), and sodium bisulfite (Acros) were used as received. Nano pure water (resistivity >18 Ω cm) was used to prepare the solution mixtures. Benzoquinone (TCI America, 98%) was purified by sublimation to obtain bright yellow crystals and subsequently used in the product identification analyses.

2.1.1. Synthesis of TiO_2–SiO_2 mixed oxides (HTS-01 to HTS-06)

A series of TiO_2–SiO_2 mixed oxide sols were prepared by simultaneous hydrolysis and condensation of TEOS and (Ti(^{i}OPr)$_4$) and varying the co-solvents. In a typical synthesis to obtain titania–silica mixed oxides with the molar ratio of Ti:Si = 1:1, 1.65 mL of TEOS was added slowly into a solution containing 9 mL of co-solvent dissolved in 9 mL of EtOH under vigorous stirring in a Teflon liner. The hydrolysis process was initiated by the introduction of 1 mL of H_2O and the process was catalyzed by the addition of 100 μL of conc. HNO_3. (Ti(^{i}OPr)$_4$) was added drop wise to ensure homogenous distribution and the suspension left to stir until gelation. The resultant gels were subjected to hydrothermal treatment in a Thermolyne autoclave reactor furnace and heated to a temperature of 120 °C for 14 h. The gelatinous precipitate attained was filtered, washed, and oven dried at ~80 °C for 9 h. These powders were then ground and calcined in static air at 500 °C for 6 h at a heating rate of 3 °C min^{-1}.

2.1.2. Synthesis of pure TiO_2 (HTS-07)

The sample HTS-07 (containing only TiO_2) was prepared as a control by adding the titania precursor (Ti(^{i}OPr)$_4$) into a mixture of 9 mL of EtOH and 9 mL of toluene, and 100 μL of conc. HNO_3 under stirring at 300 rpm followed by the drop wise addition of 1 mL of water with rapid stirring till gel formation. It was then subjected to hydrothermal treatment in an autoclave at 120 °C for 14 h. The gelatinous precipitate attained was filtered, washed, oven dried at ~80 °C for 9 h, then ground and calcined by heating in air at 500 °C for 6 h at heating rate of 3 °C min^{-1}. The product obtained was a white powder.

2.2 Characterization

Powder X-ray diffraction patterns were recorded at ambient conditions using a Rigaku Ultima IV instrument with Cu *K*α radiation (λ = 1.5408 Å), operated at an accelerating voltage of 40 kV, and emission current of 44 mA. The scanned range was between $2\theta = 20°$ and 80° with a step size of 0.02° and the scan speed was 1° min^{-1}. The crystallite sizes of the titania phase in the mixed oxide materials were determined by applying the Debye-Scherrer equation to the peaks at $2\theta = 48.3°$, 62.9°, and 75.4°. The diffraction patterns were analyzed using PDXL software provided by Rigaku. Raman spectra

were recorded using a Horiba Jobin Yvon LabRam ARAMIS spectrophotometer with an internal He–Ne (532 nm) excitation laser. The unfiltered beam of scattered laser radiation was focused onto the sample through a microscope objective (×50) for an acquisition time of 10 s and repetition of 10×. The radiation was then dispersed by a 1800 line/mm grating onto the CCD detector. Physisorption properties of the calcined mixed oxides were investigated by using the Quantachrome Nova 2200e surface area and pore size analyzer. The materials were dried overnight at 70 °C followed by extensive degassing at 100 °C and the N_2 adsorption–desorption isotherms were obtained at 77 K. Fourier Transform-Infrared (FT-IR) spectra were collected using a Bruker instrument model ALPHA equipped with ATR platinum diamond module of spectral range capabilities from 4000 to 400 cm^{-1} to further support the absence of solvents in the resulting mixed oxide materials. Optimal measurements were obtained by taking 24 scans at a resolution of 4 cm^{-1}. Surface areas were calculated using the Brunauer–Emmett–Teller (BET) equation within the relative pressure P/P_0 range of 0.05–0.30. The pore volume was obtained from the nitrogen amount adsorbed at the highest relative pressure $P/P_0 \approx 0.99$. The pore size distribution was determined by applying the Barrett–Joyner–Halenda (BJH) equation to the desorption isotherm.

The diffuse reflectance spectra (DRS) were obtained in the range between 190 and 700 nm using a Carry 100 Bio UV–Vis spectrophotometer equipped with a Harrick DR praying mantis accessory. X-ray Photoelectron Spectroscopy (XPS) studies were carried out using a custom-designed Kratos Axis Ultra system in an effort to interpret the chemical environment of the oxide species present on the surface of the photocatalysts. Survey scans were collected using energy scan range of 1200 to 25 eV, pass energy of 160 eV, step size of 1 eV. High resolution spectra were attained in the region of interest with energy window of 20–40 eV, pass energy of 20 eV, step size of 0.1 eV. The absolute energy scale was calibrated to the C 1s peak at a binding energy of 284.6 eV since this minimizes any errors in sample charging effects. The CASA XPS software was used to perform the de-convolution of the XPS peaks. A Tougaard-type background was subtracted from each spectrum to minimize the noise from scattering electrons. The surface charge of the mixed oxide materials was measured by auto titration using a zetasizer analyzer and adjusting the pH of the mixed oxide-electrolyte (KNO_3 in DI water) suspension. A Malvern NanoZS-90 zetasizer was used to measure the zeta (ζ)-potential of the mixed oxides. Deionized water was used as the diluent. Test samples were prepared in the concentration of 1 mg mL^{-1} by dispersing known amounts of the samples in aqueous 0.01 M KNO_3 solution. The pH was controlled by addition of 0.1 M KOH and/or HNO_3, and the results obtained provided useful information pertaining to the mode of adsorption of phenol molecules on the surface of mixed oxide materials.

TEM images were recorded on a Tecnai G^2 instrument operating at 120 kV. First, 5 mg of samples were dispersed in 20 mL of ethanol by sonicating for 10 to 15 min and then 2 to 3 drops of the dispersed nanoparticle suspension were deposited on C-film coated copper TEM grids (200 mesh) and allowed to air dry overnight prior to analysis.

2.3 Photocatalytic experiments

The photocatalytic activity of the mixed oxide materials was determined by the following procedure. 100 mg of photocatalyst was suspended in 100 mL of 2×10^{-4} M phenol (initial pH = 4–6) solution in a quartz cylindrical jacket reactor, and stirred in the dark at 300 rpm for 30 min under O_2 purge (60 mL min^{-1}) to establish the adsorption–desorption equilibrium. Subsequently, UV light was supplied by a Xenon arc lamp (Newport 1000 W) through a Pyrex glass filter (cut off 280 nm) and the reaction temperature was maintained at 25 ± 2 °C by channeling water in-between the walls of the reactor throughout the course of the 6 h experiment. The light intensity in the reaction medium was estimated to be ~95 mW cm^{-2}. 15 mL of the reaction mixture was withdrawn at 30 min intervals, centrifuged at 3200 rpm for 15 min, filtered through 0.45 μm Millipore filter membrane, and the clear filtrate was analyzed for organic content.

In order to investigate the role of oxygen to the catalysis reaction, experiments were carried out under N_2 flow (absence of oxygen). In addition, by applying the fluorescence technique that detects the amount of ·OH formed on irradiated TiO_2–SiO_2 surfaces using terephthalic acid (TPA) as a chemical trap for the ·OH radicals, the influence of hydroxyl radicals (·OH) on the photocatalytic reaction was studied. These radicals are known to react readily with TPA to produce highly fluorescent 2-hydroxyterephthalic acid. 20 mg of photocatalyst were added to 50 mL of 5×10^{-4} M TPA solution in 2×10^{-3} M NaOH, prior to UV irradiation. 3 mL aliquots were drawn every 20 min for a duration of 120 min, filtered through a 0.45 μm Millipore filter membrane, and the clear solution was analyzed using Flouromax-4 (JY Horiba) fluorometer. The fluorescence emission intensity of the 2-hydroxyterephthalic acid produced a peak at 425 nm after excitation at 315 nm. The intensity of the peak at 425 nm is expected to be proportional to the amount of ·OH formed. An additional experiment was carried out using triethanolamine (TEA) to study the influence of holes (h^+) in the formation of hydroxyl radicals. For that, 3.3 mL of 500 mM of TEA was added to the photocatalyst suspension containing phenol and irradiation carried out as described previously.

2.4 Analytical techniques

Elucidation of the remnant carbon content was carried out by using Shimadzu TOC-V CSH total organic carbon analyzer immediately after filtration to confirm the catalytic activity of the mixed oxides. In addition, high performance liquid chromatography (HPLC) studies was carried out using Spectra Physics 8800/8810 LC Pump equipped with a Spectra 100 UV–Vis detector to identify the degradation products as an evaluation of the catalytic activity of the hydrothermally synthesized TiO_2–SiO_2 mixed oxides. Reverse phase C18, 5 μm particle size, 250 mm length, and 4.6 mm internal diameter column was used for the separation of eluent. A mobile phase composition of 40% methanol/60% H_2O/1% glacial acetic acid was utilized and argon was purged to minimize auto-oxidation of the degradation products. The mobile phase was delivered at a flow rate of 1.0 mL min^{-1} and the detection wavelength was set at 254 nm. The reaction intermediates were confirmed by the co-injection of commercial standards under the same operating conditions. Quantitative estimates of the intermediates were obtained by using the calibration plots prepared for maleic acid (MA), fumaric acid (FA), pyrogallol (PG), hydroquinone (HQ), catechol (CC), benzoquinone (BQ), and phenol (PhOH).

2×10^{-4} M stock solution of phenol and other intermediates (excepting HBQ) was prepared and followed by serial dilution to prepare test solutions of concentrations in the range from 1.25×10^{-5} M to 2×10^{-4} M to obtain calibration plots. Due to the unavailability of commercial hydroxybenzoquinone (HBQ), the BQ calibration plot was utilized to estimate the quantity of HBQ in accordance with a previous report [43]. Thus, the given concentrations for HBQ should be interpreted with caution and may not be absolute. However, they provide guidance and indicate relative trends when comparing the reactivity of a series of photocatalysts.

3 Results and discussion

Fig. 1 represents the long-range X-ray diffractogram of hydrothermally synthesized samples, HTS-01 (prepared using

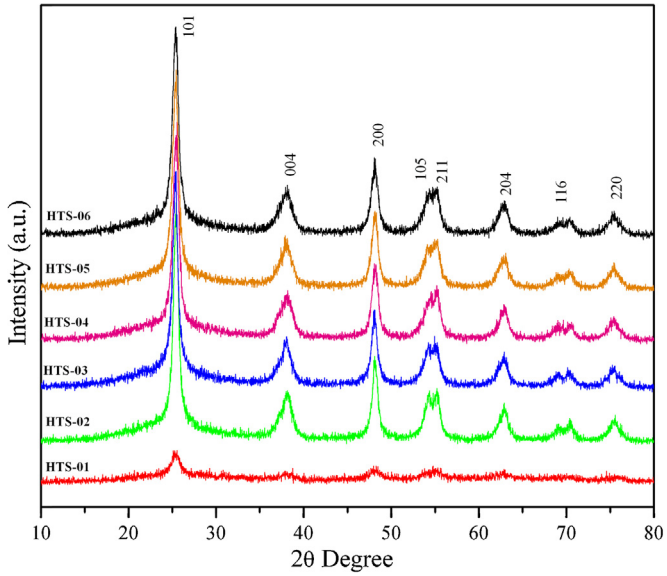

Fig. 1. X-ray diffraction pattern of TiO_2–SiO_2 mixed oxides, HTS-01 prepared solely in ethanol solvent and other mixed oxides prepared in the presence of pentane, nonane, benzene, toluene and *p*-xylene as co-solvents represented by HTS-02, HTS-03, HTS-04, HTS-05, and HTS-06, respectively. HTS refers to hydrothermal titania–silica.

ethanol only), HTS-02, HTS-03, HTS-04, HTS-05, and HTS-06 prepared using pentane, nonane, benzene, toluene, and *p*-xylene as co-solvents, respectively. HTS-01 prepared in the absence of co-solvent displays peaks with relatively low intensity suggesting low crystallinity of the titania phase. On addition of co-solvents such as pentane, nonane, benzene, toluene, and *p*-xylene a marked improvement in the diffraction contrast and narrowing of peaks are observed. The increase in the intensity of the peaks due to the anatase phase may be due to higher crystallinities and/or larger crystallite size of titania. The crystallite size of titania is estimated to be 34 Å for the titania-silica sample prepared in ethanol compared to between 42 and 46 Å for samples prepared in the presence of co-solvents as noted in Table 1. Thus, the crystallite sizes of titania in the mixed oxide materials are fairly close and the differences in the intensities of the peak are probably due to the differences in the crystallinities of the titania phase in the mixed oxide materials. In addition, TEM studies of the mixed oxide samples prepared using the non-polar solvents show the presence of lattice fringes due to titania phase indicating higher crystallinities for the titania phase whereas the titania–silica sample prepared in ethanol only do not show any lattice fringes due to titania indicating lower crystallinity.

The materials exhibit peaks due to d_{101}, d_{004}, d_{200}, d_{105}, d_{211}, d_{204}, d_{116}, and d_{220} at values of $2\theta = 25.5^\circ$, 37.9°, 48.3°, 54.3°, 55.2°, 62.9°, 69.1°, and 75.4°, respectively, corresponding to the anatase phase. In addition, the bare titania (HTS-07) was also prepared for comparison purposes and exhibits high intensity diffraction peaks (Fig. S1) depicting the high crystallinity of the titania phase in this material. The crystallite size of titania in the pure material (HTS-07) is higher (87 Å) in comparison to the titania–silica samples (34 to 46 Å) suggesting that the silica phase constricts the growth of anatase crystallites.

The presence of anatase phase and the crystalline nature of the TiO_2 phase are further supported by Raman studies as shown in Fig. S2 for representative samples HTS-02 (titania silica mixed oxide material) and HTS-07 (bare titania). The materials studied exhibit peaks at 638, 510, and 391 cm^{-1} corresponding to $E_{g(3)}$, $B_{1g(2)}$, and $B_{1g(1)}$ symmetry modes [50], respectively. An additional shoulder was observed at 197 cm^{-1} which may be due to the $E_{g(1)}$ symmetric modes. The Raman spectrum of HTS-02 (and other mixed oxide materials, not shown for the sake of clarity) show peaks with weaker intensities compared to the bare titania sample (HTS-07). This is consistent with powder XRD results indicating the high crystallinity of the bare titania containing material in comparison to the mixed oxide materials.

No peaks due to silica are observed in the powder XRD measurements indicating that the silica phase is amorphous. This is consistent with our previous observations [51]. Thus, powder XRD and Raman studies of TiO_2 and TiO_2–SiO_2 mixed oxide materials suggest that incorporation of silica alters the crystallinity and crystallite size of titania. However, the presence of silica can be inferred from Fourier transform-infrared spectroscopic (FT-IR) analysis (Fig. S3). The bands near 426, 554, and 1068 cm^{-1} are due to Ti–O–Ti bending, Si–O–Si bending, and Si–O–Si stretching, respectively. In addition, a small shoulder is seen at 934 cm^{-1}. This is assigned to Si–O–H groups. Some studies have attributed the band in the region between 930 and 960 cm^{-1} to the presence of Ti–O–Si heterolinkages, however a pure silica material also indicates a band near this region. Thus, due to the significant overlap, the existence of Ti–O–Si bands cannot be confirmed by FT-IR studies. Thus, we have performed XPS studies to verify the presence of Ti–O–Si bands.

The nitrogen isotherms of TiO_2–SiO_2 mixed oxides prepared in the presence of different co-solvents are shown in Fig. 2A. All the materials exhibit a type IV isotherm which is characteristic of mesoporous materials. Monolayer adsorption is portrayed in the initial part of the isotherm and as the relative pressure increases, multilayer adsorption and subsequent capillary condensation occurs [52]. Typically, the filling and emptying of pores takes place at separate relative pressure values resulting in hysteresis, which is a reflection of the degree of pore connectivity in these materials. All the materials prepared in this study results in H3 type hysteresis loop classification, and the results are summarized in Table 1. H3 isotherms do not exhibit limiting adsorption that levels off at higher relative pressures suggesting that the materials are comprised of

Table 1
Textural properties and activity of TiO_2–SiO_2 mixed oxide materials.

Catalysts	Co- solvent	S_{BET} ($m^2\ g^{-1}$)	PV ($cm^3\ g^{-1}$)	PD(Å)	BJH (Å)		ASC ($m^2\ g^{-1}$)	Crystallite size (Å)	Crystallinity (intensity of d_{101})	% Degraded 120 min
HTS-01	Ethanol	282	0.22	31	37		47.40	34	90	24
HTS-02	Pentane	407	0.72	71	98		58.89	46	574	100
HTS-03	Nonane	434	0.45	42	30	187	68.00	45	541	93
HTS-04	Benzene	433	0.62	57	66		40.70	42	544	64
HTS-05	Toluene	423	0.73	69	42	80	34.81	46	546	66
HTS-06	*p*-xylene	443	0.78	71	49	112	41.15	43	518	57
HTS-07	Toluene	65	0.23	141	65		–	87	767	100

HTS refers to hydrothermal titania–silica and the numbers convey chronological order. HTS-01 was prepared in ethanol and the ratio of solvent/co-solvent = 1:1 (v/v ratio) for the rest of the materials. S_{BET} refers to surface area, PV to pore volume, PD to average pore diameter which is calculated from the formula $PD = 4PV/S_{BET}$, BJH refers to pore size distribution determined by applying the BJH equation to the desorption isotherm. ASC is the Apparent Surface Coverage of Ti–O–Si species (calculated as discussed in the manuscript). The percent degradation was calculated from LC studies. The mixed oxide materials prepared in 1:1 ratio of Ti:Si and HTS-07, bare titania, is also shown for comparison.

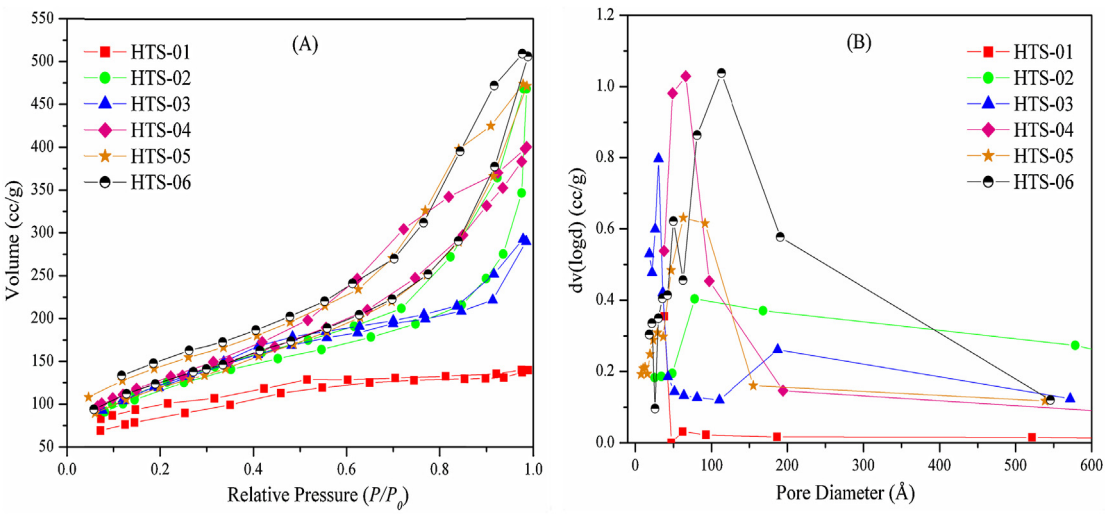

Fig. 2. (A) Nitrogen isotherms and (B) pore-size distributions of TiO_2–SiO_2 mixed oxides, HTS-01 prepared solely in ethanol solvent and other mixed oxides prepared in the presence of pentane, nonane, benzene, toluene and *p*-xylene as co-solvents represented by HTS-02, HTS-03, HTS-04, HTS-05, and HTS-06, respectively.

loose aggregates of plate-like particles with slit-like pores. The moderate change of the desorption branch is indicative of delayed evaporation of the liquid and thus gradual closure of the loop. Bimodal pore-size distributions were obtained for some materials (HTS-03, HTS-05, and HTS-06) and the results are depicted in Fig. 2B for the samples prepared with varying the type of co-solvents. Adjustment of porosities is achieved by simply changing the type of co-solvents. Si-alkoxides such as TEOS exhibit slow hydrolysis since the partial charge of Si is +0.32, whereas Ti-alkoxides like titanium isopropoxide undergo rapid hydrolysis (since the partial charge of Ti is +0.61) and a combination of these two precursors is susceptible to undergo hydrolysis at different rates leading to inhomogeneous distribution of titania in the mixed oxide materials. Thus, pre-hydrolysis of Si-alkoxide is often required to ensure equal rates of the hydrolysis of the silica and the titania precursors. Alternately, one could slow down the hydrolysis of the titania precursor by complexing them with solvents. The use of polar solvents may result in rapid precipitation to produce agglomerated phases and highly condensed products [53]. In place of incorporation of expensive surfactant templates that may introduce residual ions into the mesostructure, the use of non-polar aromatic co-solvents is an alternative method to reduce the reactivity of the Ti-alkoxide [54]. It is postulated that the conjugated π-system in the non-polar aromatic co-solvent may donate electrons to the alkoxide, and partially weaken the alkoxide bridges, improve molecular mixing in the solvent system, and subsequently form more homogeneous polymeric gels [55] that lead to good dispersion of the titania species in the silica matrix. The added advantage of the non-polar co-solvent system is minimization of the surface tension of the pore walls resulting in the formation of more open porous structures of larger interstitial spaces and high surface area [25,51]. This has been noted in the fact that HTS-01 (prepared using only ethanol) shows relatively lower surface area ($282\ m^2\ g^{-1}$) compared with the other mixed oxide materials prepared in the presence of non-polar co-solvents. The surface areas of the mixed oxide materials lie between 407 and $443\ m^2\ g^{-1}$ as depicted in Table 1 indicating the beneficial use of non-polar co-solvents in enhancing the surface areas.

Band gap estimates of the mixed oxides were determined using the UV–visible diffuse reflectance spectroscopy (Fig. 3A). The materials exhibited absorptions below 400 nm, which is attributed to electron transitions from the valence band to the conduction band. The bandgap energies were calculated from the Tauc plot, which transformed Kubelka–Munk function *vs.* the energy plots shown

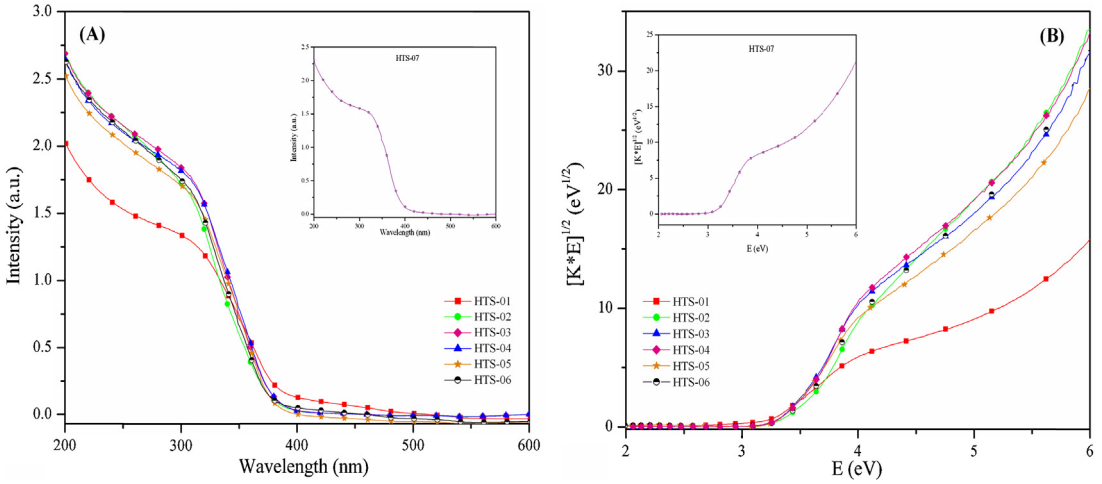

Fig. 3. (A) DRS plot and (B) Tauc plots of TiO_2–SiO_2 mixed oxides, HTS-01 prepared in ethanol solvent and other mixed oxides prepared in the presence of pentane, nonane, benzene, toluene and *p*-xylene as co-solvents represented by HTS-02, HTS-03, HTS-04, HTS-05, and HTS-06, respectively. Inset shows the plots of bare titania (HTS-07).

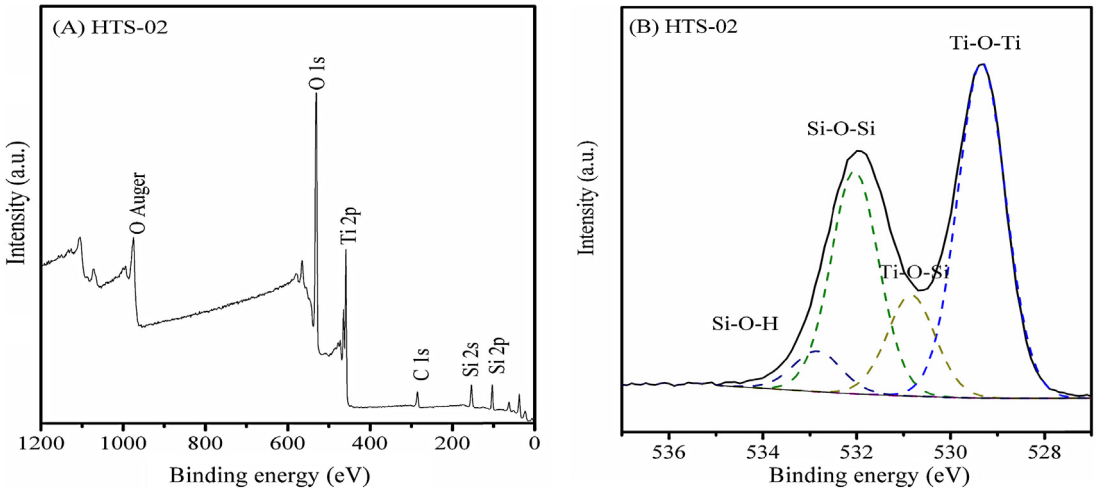

Fig. 4. (A) XPS survey spectra and (B) deconvoluted O 1S spectra of HTS-02 prepared in the presence of co-solvent pentane.

in Fig. 3B. All the mixed oxide materials had bandgap in a narrow range between 3.00 and 3.33 eV.

The TEM images (Fig. S4) illustrate the high porosities and the aperiodic nature of the mixed oxide materials and confirm the results obtained from the nitrogen physisorption studies. The absence of lattice fringes in HTS-01 (Fig. S4B) indicates low crystallinity of titania in HTS-01. In contrast, HTS-02 shows lattice fringes with d spacings of 3.54 Å due to d_{101} spacing of anatase indicating higher crystallinity. The other titania–silica samples also show similar behavior as HTS-02.

4 Photocatalytic degradation of phenol

The photocatalytic degradation efficiencies of a series of hydrothermally synthesized titania–silica mixed oxide materials were established by using phenol (initial conc. ~14–21 ppm) as a model pollutant. The amount of organics remaining in solution after irradiation was quantified by TOC analysis and the degradation products were identified by HPLC analysis.

Table 1 summarizes the results obtained from nitrogen adsorption, XPS, powder XRD, and photocatalytic experiments. The photocatalytic activity of a material is dependent on a number of factors (not limited to) that include morphology, crystal orientation, crystallinity, porosity (surface area and pore size), crystallite size, light absorption capacity, and surface composition (Ti–O–Si heterolinkages in this work). The present work provides an opportunity to examine the influence of the last five factors and we discuss their contributions systematically, towards the photocatalytic degradation of phenol in the following next paragraphs.

The degradation reactions were monitored at 30, 60, 90, 120, 180, and 360 min of irradiation. The trends in the photocatalytic activities were found to be similar when either 30, 60, 90 min or 120 min are used for comparison. However, the % degraded after 120 min from the LC analysis is chosen to illustrate the competitive role of crystallinity, porosities, crystallite size, and the active Ti–O–Si heterolinkages in the photocatalytic degradation of phenol in these mixed oxide systems. This time was chosen to allow for meaningful comparisons in efficiency because complete degradation of phenol is exhibited by two of the photocatalysts *i.e.* HTS-02 and HTS-07 when irradiated for more than 120 min. Also, the HPLC results in Tables S1–S6 of the supplementary information indicate negligible amounts of phenol remaining in solution for 5 samples (HTS-01, HTS-03 to HTS-06) when irradiated for over 120 min. Thus, the choice of 120 min allows for meaningful comparisons to understand the underlying factors responsible for the differences in the photocatalytic activities and obtain a structure–activity relationship.

The simultaneous control of crystallinity and surface area of mixed oxide TiO_2–SiO_2 catalysts has been regarded as challenging [56,57] but this work demonstrates how the presence of different co-solvents permits the modulation of both structural features in these binary oxide composites, and in addition, allows for the examination of the role of several factors that affect the photocatalytic degradation of phenol.

Table 1 indicates that HTS-01 prepared solely in ethanol showed only 24% degradation after 120 min of irradiation. Examination of the powder XRD results (Fig. 1) suggests that the intensity of the most prominent peak (d_{101} of the anatase phase) is the lowest in this titania–silica sample in comparison to the other titania–silica samples (HTS-02 to HTS-06). The addition of co-solvents such as pentane, nonane, benzene, toluene, and *p*-xylene results in materials, HTS-02 to HTS-06, exhibiting higher crystallinity of the anatase phase as depicted by an increase in the d_{101} peak intensity from 90 to values greater than 500 (the powder XRD measurements were conducted under identical experimental conditions and sample preparation methods were similar making it possible to make a realistic comparison). In addition, as discussed previously, the TEM figure (Fig. S4B) indicate higher crystallinity of the titania phase in the samples prepared in the presence of co-solvents (TEM of one representative sample HTS-02 is shown in order to avoid duplication) in comparison to HTS-01. These materials (HTS-02 to HTS-06) of enhanced crystallinity demonstrate a marked improvement in percentage degradation of phenol to between 57% and 100% in the same duration (120 min). Crystallinity is an important parameter that affects the photocatalytic activity since amorphous materials contain larger amounts of defects that can act as charge-carrier recombination sites and lower the photocatalytic efficiencies. Hence, titania–silica materials that are more crystalline (HTS-02 to HTS-06) possess higher photocatalytic activity in comparison to HTS-01 and our results are consistent with our previous observation [25]. In addition, HTS-07 (TiO_2 only) demonstrated very high activity despite having low surface area (65 $m^2\ g^{-1}$) with complete degradation after 120 min. The enhanced crystallinity of titania (d_{101} = 767) is a major contributor to the high activity. Thus, it seems that the modulation of the crystallinity of titania by the silica phase in the mixed oxides affects the photocatalytic activity.

A modest increase in the crystallite size of titania from 34 Å for the sample prepared in ethanol only to an average of 45 Å (for samples prepared in the presence of co-solvents) is also noted in Table 1. Since the crystallite sizes of titania are fairly close among

the titania–silica samples and in a narrow range, this does not seem to be a factor affecting the degradation of phenol in this study.

Surface area increments from 282 $m^2 g^{-1}$ to values greater than 405 $m^2 g^{-1}$ is also noted in the mixed oxide materials prepared in the presence of co-solvents suggesting the utility of non-polar solvents in minimizing pore collapse. Thus, the use of non-polar solvents results in the formation of highly porous mixed oxides with enhanced surface areas, pore volumes, and pore diameters as depicted by the data in Table 1. The average pore diameters also seem to increase slightly in diameter from 31 Å to sizes greater than 40 Å. BJH analysis reveals that in some cases (HTS-03, 05, and 06), bi-modal pore size distributions (with larger diameters in the range 80–187 Å) are attained for the co-solvent based materials. The higher photocatalytic activities of the samples HTS-02 to HTS-06 in comparison to HTS-01 may also be due to the presence of larger pores. Also, the pure titania sample (HTS-07) possesses a large pore diameter in comparison to HTS-01. These larger pores of varied sizes are opportune for easier access of phenol molecules, intermediates, and products to and from the active sites during the photocatalytic reactions, resulting in their enhanced degradation.

The light absorption capacity of a photocatalyst is also an important parameter that influences the photocatalytic activity. The DRS results indicate that there is a direct correlation between the absorption of the photocatalysts in the UV region and the activity. Among the mixed titania–silica samples, HTS-02 to HTS-06 possess higher absorption in the UV region of 280–320 nm and thus the higher photocatalytic activities of these 5 samples in comparison to HTS-01 is also attributed to their intrinsic capacity to absorb more light in the UV region of the incident radiation (280–320 nm).

Our results thus far indicate that, titania–silica materials (HTS-02 to HTS-06) that have higher crystallinity (to minimize electron–hole recombination), higher absorption in the UV region of interest (280–320 nm), and higher porosity (conducive to enhanced diffusion of phenol molecules) have higher photocatalytic activity compared to HTS-01.

We have thus far discussed the activities of the titania–silica photocatalysts prepared in the presence of co-solvents and that of pure titania and compared them with the titania–silica sample prepared in ethanol only. Although, the co-solvent induced photocatalysts show similar crystallite size (of titania) due to confinement by the silica phase, they demonstrate varied photocatalytic performances. We suggest that the variations in the photocatalytic activities among the titania–silica photocatalysts prepared using co-solvents (HTS-02 to HTS-06) are mainly due to the differences in the apparent surface coverage (ASC) of active Ti–O–Si linkage as discussed in the following paragraphs.

Ti–O–Si heterolinkages have been implicated previously in photocatalytic reactions [12,58] and in this work we have quantified them in our titania–silica materials to better understand the photocatalytic behavior of these mixed oxide materials. The heterolinkages (Ti–O–Si) sites activate the oxidation of phenol through strong Bronsted acid sites, and in addition, oxidative intermediates may be produced by the proximate titania interfaced with the Ti-O-Si heterolinkages. The percentage surface content of Ti–O–Si was calculated as described as follows. The O 1s transition was fit to two peaks near 530 eV [59] and 532 eV [60]. De-convolution of the broad bands between 530 and 532 eV led to three additional peaks. The band near 531.7 eV due to Ti–O–Si species [59,61,62] were quantified using Gaussian/Lorentzian shape GL (30:70) curves with equivalent eV at the full-width-half-maximum (fwhm). In order to normalize for the differences in specific surface areas (SSA), these percentages were multiplied by the SSA to obtain the apparent surface coverage (ASC). Fig. 4 shows a representative XPS survey spectra and the de-convoluted O 1S spectra of the most active co-solvent based mixed oxide photocatalyst, HTS-02, which was prepared in the presence of co-solvent pentane (other plots are displayed in the supplementary information, Figs. S5 and S6). Among the 5 titania–silica samples prepared in the presence of co-solvents, the samples HTS-02 and HTS-03 show higher activities for degradation of phenol in comparison to the other 3 samples (HTS-04, HTS-05, and HTS-06). The comparatively higher ASC (58.9 $m^2 g^{-1}$ for HTS-02 and 68.0 $m^2 g^{-1}$ for HTS-03) is suggested as being responsible for the higher degradation efficiencies of 100% and 93%, respectively in these samples. In contrast, the samples HTS-04, HTS-05, and HTS-06 have ASC's in the similar ranges with values of 40.7, 34.8, and 41.15 $m^2 g^{-1}$, respectively. The amount of phenol degraded after 120 min of irradiation in these samples was found to be 64%, 66%, and 57%, respectively.

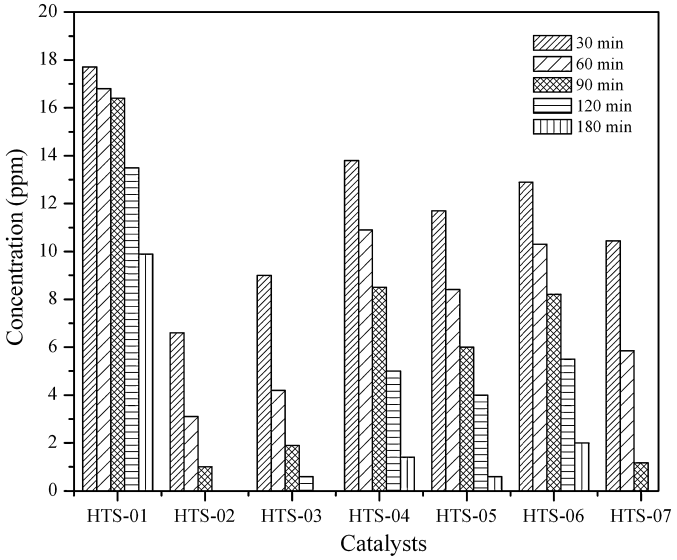

Fig. 5. Concentration of phenol (ppm) remaining in solution determined by HPLC at 30, 60, 90, and 180 min for TiO_2–SiO_2 materials, HTS-01 prepared in ethanol, HTS-02, HTS-03, HTS-04, HTS-05, and HTS-06 using different co-solvents pentane, nonane, benzene, toluene, and *p*-xylene, respectively.

Fig. 5 summarizes the concentration of phenol remaining in solution after irradiation in the presence of materials prepared using different co-solvent systems. As discussed earlier, the material prepared using ethanol only (HTS-01) exhibits the lowest activity showing mere 24% degradation after 120 min. In contrast, the materials prepared using aliphatic non-polar co-solvents demonstrate higher efficiencies and almost complete degradation is achieved within 180 min mainly due to the combination of ASC and the crystallinity of those materials. Titania-silica materials prepared using aromatic co-solvents exhibit activities between 57% and 66% degradation after 120 min of irradiation.

The influence of the adsorption of phenol on the degradation efficiencies was also studied. All the photocatalysts in this study adsorbed similar amounts of phenol $\sim 2.5 \times 10^{-4}$ mol g^{-1} after 360 min of stirring in the dark. This value appears to be similar for all the photocatalysts including the sample containing TiO_2 only. This revealed that there is a negligible role of adsorption in the degradation process as inferred by Primet et al. [63]. However, the phenol uptake during this time period differs due to the different surface area of the materials. HTS-07 (TiO_2 only) shows a high phenol uptake of 4.07×10^{-6} mol m^{-2} (2.65×10^{-4} mol g^{-1}), after 360 min of stirring in the dark. This may be due to the higher positive charge on the surface (Iso Electric Point (IEP) = 7.1) as suggested by the zeta potential measurements (Fig. S7) and the much lower surface area of this material compared to that of the TiO_2–SiO_2 materials. The TiO_2–SiO_2 mixed oxide materials exhibit phenol uptake values that are less than that of pure titania (HTS-07), and lie in the range of 5.03×10^{-7}–9.05×10^{-7} mol m^{-2}.

HTS-01 shows slightly higher adsorption of phenol in the dark with a value of 9.05×10^{-7} mol m^{-2} (2.55×10^{-7} mol g^{-1}) than the other mixed oxide materials mainly due to the relatively low surface area (282 m^2 g^{-1}). HTS-02 and HTS-03 have similar IEP values of ~5.7 but HTS-02 shows a slightly higher phenol uptake of 6.92×10^{-7} mol m^{-2} compared to 5.93×10^{-7} mol m^{-2} for HTS-03, and this may be attributed to the marginally lower surface area of HTS-02 (407 m^2 g^{-1}) when compared to HTS-03 (434 m^2 g^{-1}). The other mixed oxide materials, HTS-04, HTS-05, and HTS-06 have IEP's of nearly 4.9, and similar surface areas of 433, 423, and 443 m^2 g^{-1}, respectively and show somewhat similar phenol uptakes of 5.03, 6.52, and 5.91×10^{-7} mol m^{-2} after 360 min of stirring in the dark.

The aforementioned activities were attained *via* heterogeneous photocatalysis that involves the formation of highly reactive oxidation species (ROS) such as ·OH, $\cdot OH_2$, $O_2^{-}\cdot$, H_2O_2, ·OOH, HOOH, –OH, and H_2O_2. During UV irradiation, the electrons in the TiO_2 of the mixed oxide are excited to the conduction band creating an electron–hole pair as indicated by Eq. (1). The holes may oxidize water to form hydroxyl radicals as in Eq. (2). The photogenerated electrons may react with molecular oxygen to form O_2^{-} radicals (Eq. (3)). These eventually form ·OH radicals through a series of reactions indicated by (4)–(6). Hydroxyl radicals are believed to be the major species responsible for participating in the photocatalytic degradation process [31,64,65]. Key photocatalytic reactions are indicated in Eqs. (1)–(6).

$$TiO_2 \rightarrow h^+ + e^- \quad (1)$$

$$H_2O + h^+ \rightarrow HO\cdot + H^+ \quad (2)$$

$$O_2 + e^- \rightarrow O_2^{-}\cdot \quad (3)$$

$$O_2^{-}\cdot + H^+ \rightarrow \cdot O_2H \quad (4)$$

$$2\cdot O_2H \rightarrow H_2O_2 + O_2 \quad (5)$$

$$H_2O_2 + e^- \rightarrow HO\cdot + {}^{-}OH \quad (6)$$

·OH radical attack on phenol leads to the formation of several intermediates such as hydroquinone (HQ), catechol (CC), pyrogallol (PG), hydroxyhydroquinone (HHQ), resorcinol (RC), muconic acid (MU), *p*-benzoquinone (*p*-BQ), *o*-benzoquinone (*o*-BQ), and hydroxybenzoquinone (HBQ) [43,66–69].

Additional scavenging experiments were carried out to determine the reactive oxidative species participating in the photocatalytic reactions. We chose one representative titania–silica photocatalyst (HTS-05) and compared its photocatalytic activity with pure TiO_2 (HTS-07) since these two samples were prepared using toluene as the co-solvent. The presence of TEA (h^+ scavenger) provides quite an interesting result. In the presence of TEA, phenol degradation reaction is totally inhibited in both these samples as observed by phenol peaks of somewhat similar areas in LC. However, notable increase in UV–Vis absorption spectra of irradiated solutions indicates that degradation of PhOH in the presence of TEA may convert PhOH into some other products that absorb light at similar wavelength as PhOH. This suggests that photogenerated holes (h^+) play a minimal role in the degradation of PhOH by TiO_2–SiO_2 in our experimental conditions. The photocatalytic activities of the selected catalysts in the presence of N_2 flow retain the phenol concentration around the original 15 ppm after 6 h of irradiation, which suggest that the $O_2\cdot^-$ radicals are crucial for phenol degradation.

During photocatalysis, excited electrons in the conduction band may be captured by dissolved oxygen molecules to produced superoxide radicals ($O_2\cdot^-$) that subsequently produce ·OH, which oxidize

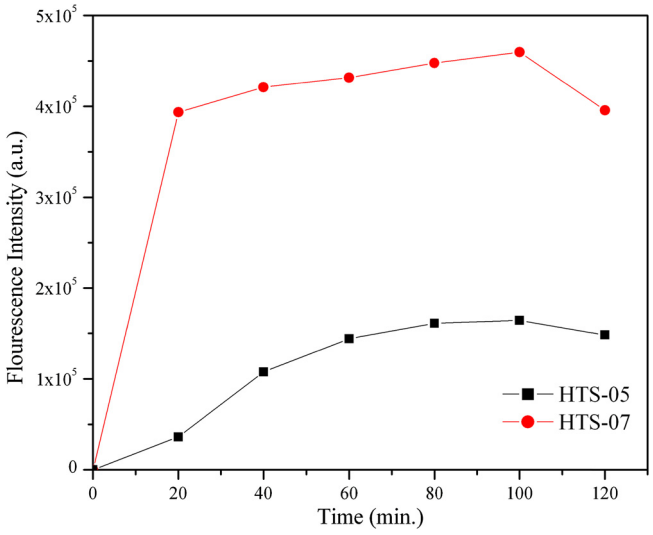

Fig. 6. Plot of 2-HTPA *vs.* time for HTS-05 (TiO_2:SiO_2 = 1:1) and HTS-07 (pure TiO_2) photocatalysts.

adsorbed organics. It is well known that ·OH radicals are believed to be the most reactive oxidative species responsible for photocatalysis. Thus, ·OH trapping experiments were carried out to estimate the formation of ·OH under UV light and understand the role of oxygen in scavenging electrons. These radicals may react with terephthalic acid (TPA) to form fluorescent 2-hydroxyterephthalic acid (2-HTPA), which in this case, is proposed to be proportional to the amount of ·OH formed. Fig. 6 shows a plot of 2-HTPA *vs.* time for selected catalysts HTS-05 and HTS-07.

The increase in fluorescence emission intensity of analyzed solutions due to the formation of 2-HTPA suggests that, the number of ·OH increases in both catalysts and the amount is maintained after 60 min. However, higher intensities were achieved for HTS-07, which suggests more ·OH radicals were produced for this photocatalyst as compared to HTS-05. These observations are consistent with the photocatalytic activity results which show that degradation efficiency of HTS-07 was higher than that of HTS-05.

Under our experimental conditions, MA, FA, PG, HQ, CC, HBQ (trace amounts for certain photocatalysts) and BQ have been identified as intermediates. It appears that the photocatalysts mainly favor CC formation rather than HQ formation as the major primary intermediate in the degradation pathway insinuating ·OH radical attack at the *ortho* position of the benzene ring. This is due to the fact that 1,2-dihydroxyl substitutions in the benzene ring are more stable than the 1,4-dihydroxyl substitutions *via* the intramolecular H-bonding. In addition, two *ortho* positions are available for attachment of a ·OH radical, resulting in the formation of CC rather than HQ. An exhibition of the *ortho–para* directing effect of phenol is thus evidenced. Although, there is a similar probability for the attachment of ·OH radical at the meta position, RC was not detected as an intermediate in our study, however, radiolysis studies suggest its detection under deaerated conditions [69].

Under acidic conditions di-hydroxybenzene (CC and HQ) and benzoquinones are in equilibrium [70]. The solution pH was detected to be between 4 and 6 implicating equilibrium between CC/HQ and BQ. This was confirmed by the formation of BQ as a major secondary intermediate from either CC or HQ. The formation of *p*-BQ was more predominant than *o*-BQ, irrespective of CC as a major intermediate. *o*-BQ is unstable in aqueous solution due to inevitable autoxidation reactions [71].

Further oxidation results in the cleavage of the benzene ring and emergence of ring opening products [27,67,72,73] such as maleic acid (MA), fumaric acid (FA), oxalic acid (OA), malonic acid

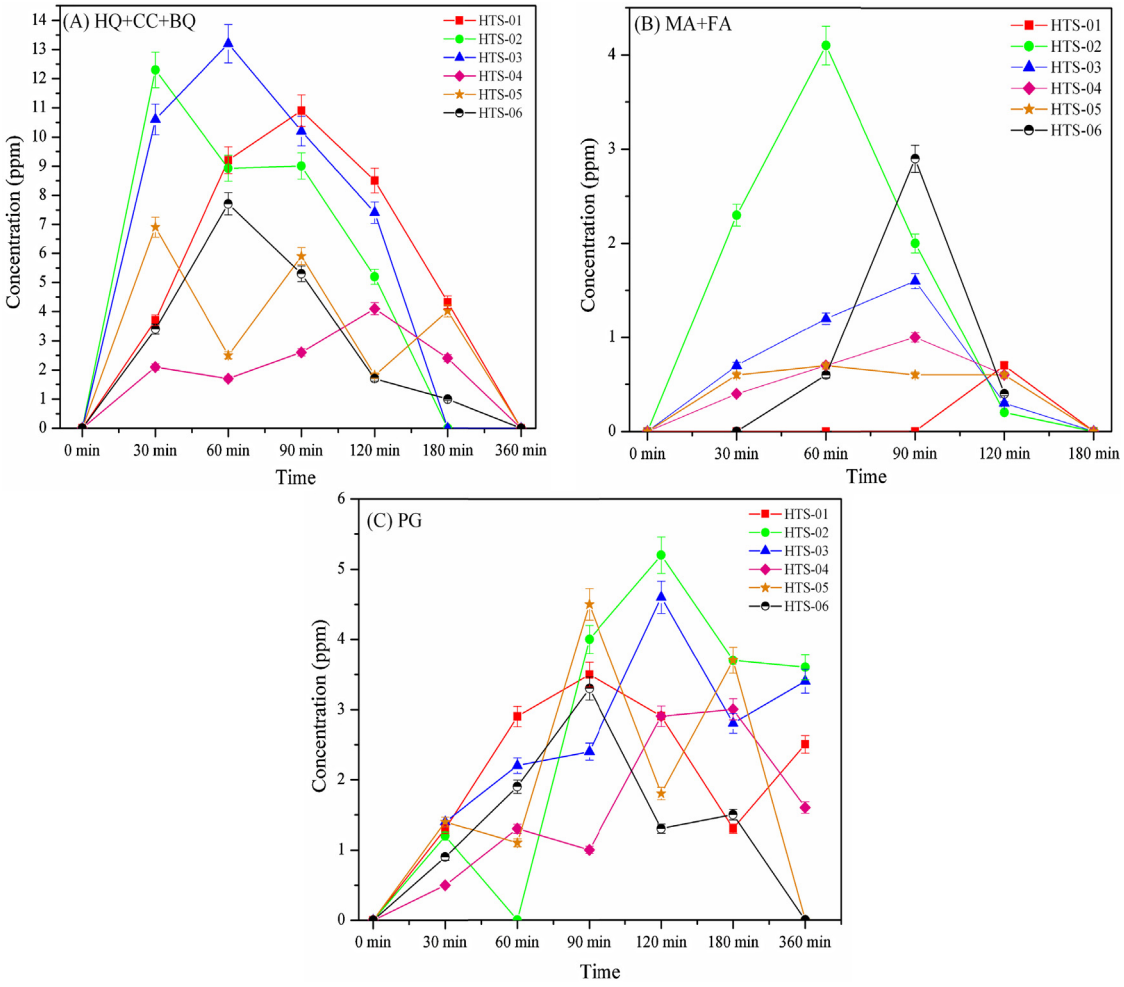

Fig. 7. Combined concentrations of intermediates (ppm) in solution, (A) hydroquinone (HQ) + catechol (CC) + benzoquinone (BQ), (B) maleic acid (MA) + fumaric acid (FA), (C) pyrogallol (PG) determined by HPLC, formed during the degradation process for the materials prepared using different co-solvents.

(MAL) and acetic acid (AcOH) [43,67,71]. In this study, MA and FA were detected with the former appearing as the more predominant minor intermediate. Further cleavage of these aliphatic carboxylic acids leads to the formation of AcOH in trace amount as evidenced by others [31,67,74]. This was confirmed by white turbidity of the reaction mixture on treatment with sodium bisulfite although no quantitative estimation was made since this was not the focus of this work. At the end of the photocatalytic experiment, the pH of the reaction mixture was found to be ~7 which also supported the complete mineralization and/or presence of very weak acid in the solution. A sample chromatogram is depicted in Fig. S8.

The quantitative calculations of the intermediates clearly show that the concentrations increased to an optimum and then decreased with time while the concentration of PhOH decreased gradually throughout the course of the experiment.

The photocatalysts studied show an increment in the concentration of intermediates during the time period of 60–90 min and then they start to decrease. All types of intermediates follow similar trends with our photocatalysts as depicted in Fig. 7. We do not see any systematic variations in the concentrations of the intermediates among the various photocatalysts. Fig. 7A shows the combined concentration of the di-hydroxybenzene (CC and HQ) and benzoquinone (BQ), which have been found as major intermediates in our studies. It appears that the concentration of the di-hydroxybenzene products is more predominant than the other intermediates. Almost all catalysts show a typical volcano type plot in the variation of the concentration of intermediates (HQ + CC + BQ) against time. Notably, the catalyst HTS-05 behaves somewhat different than the other catalysts, which may be due to the different rate of formation of the individual intermediates (CC, HQ, and BQ). This pattern also influences the formation of subsequent minor intermediates, such as tri-hydroxyl substituted benzene (PG) as shown in Fig. 7C. This may perhaps be due to the low ASC (~35 $m^2 g^{-1}$) of this sample in comparison to other samples (41 to 68 $m^2 g^{-1}$). However, the exact reason(s) for the unique behavior of this catalyst HTS-05 in this study is unknown at this moment and is beyond the scope of this work. The concentrations of opened ring carboxylic acid intermediates, such as maleic acid (MA) and fumaric acid (FA) are depicted by the graphs in Fig. 7B, and these products remain in the solution for a limited time period (~90 min), and may undergo further cleavage. PG is the only trihydroxy substituted benzene product that has been detected in this study (Fig. 7C), and it remains in the solution until 360 min when the photocatalysts HTS-01, HTS-02, HTS-03, and HTS-04 are analyzed. Complete mineralization of PhOH is achieved and negligible amounts of the intermediates are detected at the end of the degradation reaction. The concentrations of all intermediates at 30 min intervals up to 360 min are available in the supporting information from Tables S1–S6.

This manuscript provides a detailed quantitative analysis of the intermediate distribution during the photodegradation of phenol using TiO_2–SiO_2 mixed oxide materials. According to our HPLC results, we propose the mechanism *via* CC for HTS-01, HTS-04,

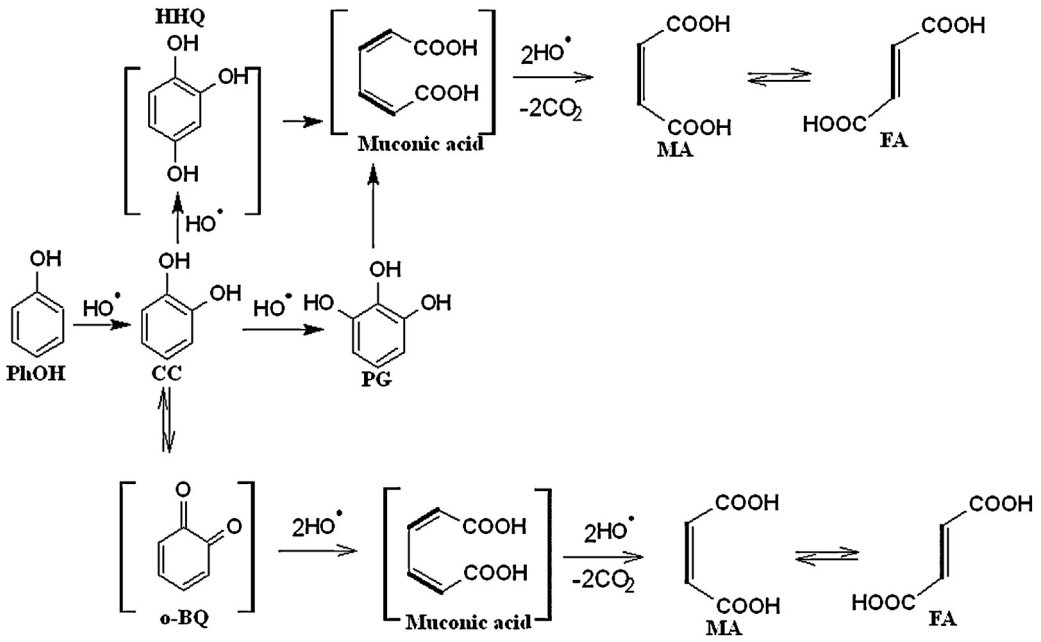

Scheme 1. Proposed reaction route for the degradation of phenol *via* CC. Further attack of the hydroxyl radical on PG leads to the ring opening products. The intermediates shown in the parentheses have not been detected under our experimental conditions.

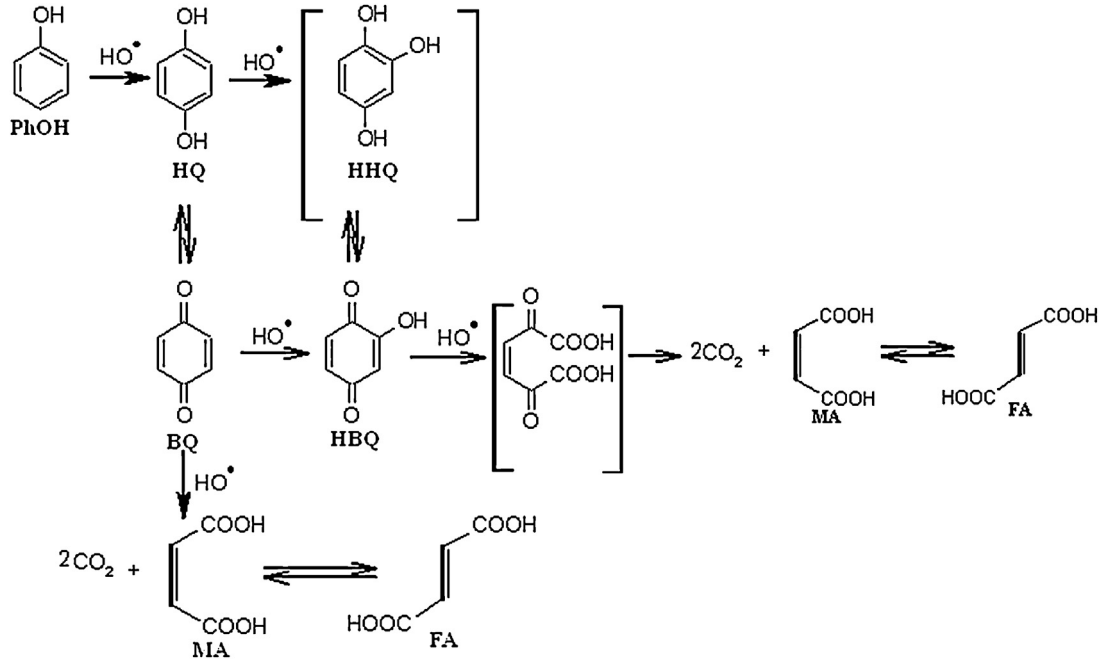

Scheme 2. Plausible reaction route for the degradation of phenol *via* HQ. Cleavage may eventually lead to the formation of CO_2 and H_2O. The intermediates shown in the parentheses have not been detected under our experimental conditions.

and HTS-06 that were prepared in ethanol, benzene and ethanol, and *p*-xylene and ethanol, respectively. The HQ pathway and/or a combination of the CC pathway is proposed for some of the photocatalysts (HTS-02, HTS-03, and HTS-05) which are prepared using pentane, nonane, and toluene as co-solvents, respectively). The possibility of HHQ is acknowledged, however, this intermediate is not detected probably due to low life time or it is produced in amounts lower than the detection limits of our instrument. However, PG, an isomeric form of HHQ was detected as one of the major secondary intermediates formed *via* the CC pathway, owing to its enhanced stability facilitated by intra-molecular hydrogen bonding.

The degradation mechanism *via* CC pathway (Scheme 1) appears to be more dominant than the HQ pathway. Scheme 2 illustrates the HQ pathway of the PhOH degradation process. In this path, the degradation begins with the addition of ·OH radical at the *para* position of the phenol that undergoes further ring opening, and finally produces MA and FA as ring opening products.

5 Conclusion

Co-solvent induced TiO_2–SiO_2 mixed oxides have been prepared successfully by hydrothermal treatment. The non-polar co-solvents generally assist in the enhancement of the crystallinity and

minimization of pore collapse. The crystallinities of the titania phase in the titania–silica mixed oxide materials were found to be increased by over five times by incorporation of non-polar solvents in the synthesis gel. Similarly, an increment in the pore diameter from 31 Å to between 42 and 141 Å was noted for the mixed oxide materials prepared in the absence and presence of co-solvents. The factors influencing the photocatalytic activity span several physicochemical properties and this study specifically demonstrated the importance of the crystallinity, pore sizes, and Ti–O–Si heterolinkages of the mixed oxides. The mixed oxide materials prepared in the presence of co-solvents showed impressive photocatalytic activities in comparison to the material prepared using a polar solvent only. Complete degradation of phenol was achieved in 2 h by a mixed oxide material that possessed high crystallinity, large apparent surface coverage of Ti–O–Si heterolinkages and large pore size (BJH). A degradation mechanism that proceeds mainly through the catechol pathway, with a small contribution from the hydroquinone pathway is proposed. It also provides evidence of catechol, hydroquinone, benzoquinone, and pyrogallol as the major intermediates while maleic and fumaric acids are minor intermediates in this reaction. TOC and HPLC results suggest complete mineralization of phenol.

Acknowledgments

We extend sincere gratitude to NSF-CHE-0619190, NSF-CHE-0722632, NSF-EPS-0903804, DE-EE0000270, NNX12AB17G, and State of SD for funding this project.

Appendix A. Supplementary data

Supplementary data associated with this article can be found, in the online version, at http://dx.doi.org/10.1016/j.apcatb.2013.11.025.

References

[1] J. Michałowicz, W. Duda, Polish Journal of Environmental Studies 16 (2007) 347–362.
[2] U. Stafford, K.A. Gray, P.V. Kamat, Journal of Physical Chemistry 98 (1994) 6343–6351.
[3] J.P. Wilcoxon, Journal of Physical Chemistry B 104 (2000) 7334–7343.
[4] K. Vinodgopal, S. Hotchandani, P.V. Kamat, Journal of Physical Chemistry 97 (1993) 9040–9044.
[5] O. Legrini, E. Oliveros, A.M. Braun, Chemical Reviews 93 (1993) 671–698.
[6] R. Thiruvenkatachari, S. Vigneswaran, I. Moon, Korean Journal of Chemical Engineering 25 (2008) 64–72.
[7] R.W. Matthews, Pure and Applied Chemistry 64 (1992) 1285–1290.
[8] C.D. Jaeger, A.J. Bard, The Journal of Physical Chemistry 83 (1979) 3146–3152.
[9] M.A. Fox, D.T. Maria, Chemical Reviews 93 (1993) 341–357.
[10] C.B. Almquist, P. Biswas, Journal of Catalysis 212 (2002) 145–156.
[11] C. Anderson, A.J. Bard, Journal of Physical Chemistry 99 (1995) 9882–9885.
[12] C. Anderson, A.J. Bard, Journal of Physical Chemistry B 101 (1997) 2611–2616.
[13] L.J. Alemany, M.A. Banares, E. Pardo, F. Martin, M. Galán-Fereres, J. Blasco, Applied Catalysis B: Environmental 13 (1997) 289–297.
[14] Y. Arai, K. Tanaka, A.L. Khlaifat, Journal of Molecular Catalysis A: Chemical 243 (2006) 85–88.
[15] N. Takeda, T. Torimoto, S. Sampath, S. Kuwabata, H. Yoneyama, Journal of Physical Chemistry 99 (1995) 9986–9991.
[16] Y. Xu, C.H. Langford, Journal of Physical Chemistry 99 (1995) 11501–11507.
[17] Y. Xu, C.H. Langford, Journal of Physical Chemistry B 101 (1997) 3115–3121.
[18] T. Torimoto, S. Ito, S. Kuwabata, H. Yoneyama, Environmental Science & Technology 30 (1996) 1275–1281.
[19] A.R. Oki, Q. Xu, B. Shpeizer, A. Clearfield, X. Qiu, S. Kirumakki, S. Tichy, Catalysis Communications 8 (2007) 950–956.
[20] G. Liu, Y. Liu, G. Yang, S. Li, Y. Zu, W. Zhang, M. Jia, Journal of Physical Chemistry C 113 (2009) 9345–9351.
[21] Y. Xu, W. Zheng, W. Liu, Journal of Photochemistry and Photobiology A: Chemistry 122 (1999) 57–60.
[22] G. Dagan, M. Tomkiewicz, Journal of Physical Chemistry 97 (1993) 12651–12655.
[23] X. Gao, I.E. Wachs, Catalysis Today 51 (1999) 233–254.
[24] C.J. Brinker, in: H.E. Bergna (Ed.), Colloid Chemistry of Silica, American Chemical Society, Washington, DC, 1994, pp. 361–402.
[25] H.S. Kibombo, D. Zhao, A. Gonshorowski, S. Budhi, M.D. Koppang, R.T. Koodali, Journal of Physical Chemistry C 115 (2011) 6126–6135.
[26] D. Chen, M. Sivakumar, A.K. Ray, Developments in Chemical Engineering and Mineral Processing 8 (2000) 505–550.
[27] J. Chen, L. Eberlein, C.H. Langford, Journal of Photochemistry and Photobiology A: Chemistry 148 (2002) 183–189.
[28] H. Al-Ekabi, N. Serpone, E. Pelizzetti, C. Minero, M.A. Fox, R.B. Draper, Langmuir 5 (1989) 250–255.
[29] A.L. Linsebigler, G. Lu, J.T. Yates, Chemical Reviews 95 (1995) 735–758.
[30] X. Li, J.W. Cubbage, W.S. Jenks, Journal of Organic Chemistry 64 (1999) 8525–8536.
[31] X. Li, J.W. Cubbage, T.A. Tetzlaff, W.S. Jenks, Journal of Organic Chemistry 64 (1999) 8509–8524.
[32] R.J. Davis, Z.F. Liu, Chemistry of Materials 9 (1997) 2311–2324.
[33] O. Alaoui, Q. Nguyen, T. Rhlalou, Environmental Chemistry Letters 7 (2009) 175–181.
[34] Y.X. Chen, K. Wang, L.P. Lou, Journal of Photochemistry and Photobiology A—Chemistry 163 (2004) 281–287.
[35] Y. Guo, S. Yang, X. Zhou, C. Lin, Y. Wang, W. Zhang, Journal of Nanomaterials (2011), Article ID 296953.
[36] C. Xie, Z. Xu, Q. Yang, N. Li, D. Zhao, D. Wang, Y. Du, Journal of Molecular Catalysis A: Chemical 217 (2004) 193–201.
[37] K.Y. Jung, S.B. Park, Applied Catalysis B: Environmental 25 (2000) 249–256.
[38] A.A. Ismail, I.A. Ibrahim, M.S. Ahmed, R.M. Mohamed, H. El-Shall, Journal of Photochemistry and Photobiology A: Chemistry 163 (2004) 445–451.
[39] C. Shifu, C. Gengyu, Solar Energy 79 (2005) 1–9.
[40] M. Brigante, P.C. Schulz, Journal of Colloid and Interface Science 363 (2011) 355–361.
[41] Y.K. Kim, E.Y. Kim, C.M. Whang, Y.H. Kim, W.I. Lee, Journal of Sol–Gel Science and Technology 33 (2005) 87–91.
[42] E. Kim, C. Whang, W. Lee, Y. Kim, Journal of Electroceramics 17 (2006) 899–902.
[43] J. Theurich, M. Lindner, D.W. Bahnemann, Langmuir 12 (1996) 6368–6376.
[44] J. Jammaer, C. Aprile, S.W. Verbruggen, S. Lenaerts, P.P. Pescarmona, J.A. Martens, Chemistry and Sustainability, Energy and Materials 4 (2011) 1457–1463.
[45] Z. Ding, C.Q. Lu, P.E. Greenfield, Journal of Colloid and Interface Science 232 (2000) 1–9.
[46] A.A. Belhekar, S.V. Awate, R. Anand, Catalysis Communications 3 (2002) 453–458.
[47] C.M. Teh, A.R. Mohamed, Journal of Alloys and Compounds 509 (2011) 1648–1660.
[48] Z. Guo, R. Ma, G. Li, Chemical Engineering Journal 119 (2006) 55–59.
[49] E. Moctezuma, B. Zermeno, E. Zarazua, L.M. Torres-Martinez, R. Garcia, Topics in Catalysis 54 (2011) 496–503.
[50] Z.Y. Wu, Y.F. Tao, Z. Lin, L. Liu, X.X. Fan, Y. Wang, Journal of Physical Chemistry C 113 (2009) 20335–20348.
[51] K.T. Ranjit, I. Martyanov, D. Demydov, S. Uma, S. Rodrigues, K.J. Klabunde, Journal of Sol–Gel Science and Technology 40 (2006) 335–339.
[52] M. Kruk, M. Jaroniec, Chemistry of Materials 13 (2001) 3169–3183.
[53] C. Sanchez, J. Livage, M. Henry, F. Babonneau, Journal of Non-Crystalline Solids 100 (1988) 65–76.
[54] J.C. Brinker, G.W. Scherer, Sol–Gel Science: The Physics and Chemistry of Sol–Gel Processing, Academic Press Inc, San Diego, 1990.
[55] M.S. Bains, D.C. Bradley, Canadian Journal of Chemistry 40 (1962) 2218–2228.
[56] D. Hufschmidt, D. Bahnemann, J.J. Testa, C.A. Emilio, M.I. Litter, Journal of Photochemistry and Photobiology A: Chemistry 148 (2002) 223–231.
[57] C.A. Emilio, M.I. Litter, M. Kunst, M. Bouchard, C. Colbeau-Justin, Langmuir 22 (2006) 3606–3613.
[58] P. Kooyman, P. Waal, P.J. Verdaasdonk, K. Jansen, H. Bekkum, Catalysis Letters 13 (1992) 229–238.
[59] B. Erdem, R.A. Hunsicker, G.W. Simmons, E.D. Sudol, V.L. Dimonie, M.S. El-Aasser, Langmuir 17 (2001) 2664–2669.
[60] M. Fukushima, Y. Zhou, Y.-I. Yoshizawa, K. Hirao, Journal of the European Ceramic Society 28 (2008) 1043–1048.
[61] M.J. Kim, K.-D. Kim, H.O. Seo, Y. Luo, N.K. Dey, Y.D. Kim, Applied Surface Science 257 (2011) 2489–2493.
[62] J. Wang, X. Liu, R. Li, P. Qiao, L. Xiao, J. Fan, Catalysis Communications 19 (2012) 96–99.
[63] M.V. Mathieu, M. Primet, P. Pichat, Journal of Physical Chemistry 75 (1971) 1221–1226.
[64] M.R. Hoffmann, S.T. Martin, W. Choi, D.W. Bahnemann, Chemical Reviews 95 (1995) 69–96.
[65] N.A. Laoufi, D. Tassalit, F. Benthar, Global NEST Journal 10 (2008) 404–418.
[66] I.G. Zenkevich, M.V. Kochetova, O.G. Larionov, A.A. Revina, Journal of Analytical Chemistry 60 (2005) 655–667.
[67] H.R. Devlin, H.J. Iestyn, Industrial & Engineering Chemistry Fundamentals 23 (1984) 387–392.
[68] U.I. Gaya, A.H. Abdullah, Z. Zainal, M.Z. Hussein, International Journal of Chemistry 2 (2010) 180–193.

[69] S. Hashimoto, T. Miyata, M. Washino, W. Kawakami, Environmental Science & Technology 13 (1979) 71–75.
[70] R. Alnaizy, A. Akgerman, Advances in Environmental Research 4 (2000) 233–244.
[71] J.A. Zazo, J.A. Casas, A.F. Mohedano, M.A. Gilarranz, J.J. Rodríguez, Environmental Science & Technology 39 (2005) 9295–9302.
[72] K.-i. Okamoto, Y. Yamamoto, H. Tanaka, M. Tanaka, A. Itaya, Bulletin of Chemical Society of Japan 58 (1985) 2015–2022.
[73] S. Gopalan, P.E. Savage, Journal of Physical Chemistry 98 (1994) 12646–12652.
[74] L. Meunier, J.F. Pilichowski, P. Boule, Canadian Journal of Chemistry 79 (2001) 1179–1186.